Article:
Smitten, K.L., Scattergood, P.A., Kiker, C. et al. (2020) Triazole-based osmium(II) complexes displaying red/near-IR luminescence : antimicrobial activity and super-resolution imaging. Chemical Science, 11 (33). pp. 8928-8935. ISSN: 2041-6520

https://doi.org/10.1039/d0sc03563g

Chemical Science

ROYAL SOCIETY OF CHEMISTRY

EDGE ARTICLE

View Article Online
View Journal | View Issue

Check for updates

Cite this: *Chem. Sci.*, 2020, **11**, 8928

All publication charges for this article have been paid for by the Royal Society of Chemistry

Received 28th June 2020
Accepted 6th August 2020

DOI: 10.1039/d0sc03563g

rsc.li/chemical-science

Triazole-based osmium(II) complexes displaying red/near-IR luminescence: antimicrobial activity and super-resolution imaging†

Kirsty L. Smitten, [a] Paul A. Scattergood, *[b] Charlotte Kiker, [a] Jim A. Thomas *[a] and Paul I. P. Elliott *[b]

Cellular uptake, luminescence imaging and antimicrobial activity against clinically relevant methicillin-resistant *S. aureus* (MRSA) bacteria are reported. The osmium(II) complexes $[Os(N\text{^}N)_3]^{2+}$ (*N*^*N* = 1-benzyl-4-(pyrid-2-yl)-1,2,3-triazole ($\mathbf{1}^{2+}$); 1-benzyl-4-(pyrimidin-2-yl)-1,2,3-triazole ($\mathbf{2}^{2+}$); 1-benzyl-4-(pyrazin-2-yl)-1,2,3-triazole ($\mathbf{3}^{2+}$)) were prepared and isolated as the chloride salts of their meridional and facial isomers. The complexes display prominent spin-forbidden ground state to triplet metal-to-ligand charge transfer (^{3}MLCT) state absorption bands enabling excitation as low as 600 nm for *fac*/*mer*-$\mathbf{3}^{2+}$ and observation of emission in aqueous solution in the deep-red/near-IR regions of the spectrum. Cellular uptake studies within MRSA cells show antimicrobial activity for $\mathbf{1}^{2+}$ and $\mathbf{2}^{2+}$ with greater toxicity for the meridional isomers in each case and *mer*-$\mathbf{1}^{2+}$ showing the greatest potency (32 μg mL^{-1} in defined minimal media). Super-resolution imaging experiments demonstrate binding of *mer*- and *fac*-$\mathbf{1}^{2+}$ to bacterial DNA with high Pearson's colocalisation coefficients (up to 0.95 using DAPI). Phototoxicity studies showed the complexes exhibited a higher antimicrobial activity upon irradiation with light.

Introduction

Over recent decades considerable attention has been paid to the use of complexes of Ru^{II}, Ir^{III} and Re^{I} d^6 transition metal ions as luminescent probes for biological imaging.[1–7] The long-lived triplet metal-to-ligand charge transfer (^{3}MLCT) excited states responsible for the emission from these complexes can also sensitise singlet oxygen production which provides a basis for applications in photodynamic therapy (PDT) and the development of theranostic probes.[8–11] A noticeable drawback of these systems is their relatively high photoexcitation energy, which can result in unintended cellular damage during imaging and also limits the depth of tissue penetration. Consequently, cell-permeant luminescent imaging agents which display both low-energy electronic absorption features and deep-red phosphorescence, thus permitting excitation and luminescence imaging within the biologically-transparent region of the visible spectrum, are attractive synthetic targets.[12–14]

Osmium(II) complexes offer several advantages over their ruthenium(II) analogues. The high spin–orbit coupling constant associated with Os^{II} facilitates formally forbidden direct transitions from the ground state into ^{3}MLCT excited states, resulting in associated absorbance bands of appreciable intensity in their optical spectra, often extending out to 700 nm.[15] Excitation into these low energy absorptions results in deep-red to near-infrared (NIR) phosphorescence ($\lambda_{em} \approx$ 650–900 nm) and given that they are also highly kinetically inert, Os^{II} complexes offer significant potential as cellular imaging agents.[16] However, despite these favourable attributes, the use of Os(II) complexes as phosphorescent biological probes is still relatively scarce.

The Keyes group has reported the cellular uptake and imaging of a polyarginine-conjugated osmium(II) imidazophenanthroline complex[17] as well as live-cell imaging of a mitochondria-targeting Os^{II} bis-(4-carboxyphenyl-terpyridine)-derived complex.[18] The Zhang group has investigated a benzimidazole-containing Os^{II} complex as a NIR emissive lysosomal tracker,[19] as well as a related complex that enables NIR luminescence imaging of the RNA within the nucleus of live cells.[20] Very recently Zhu *et al.* have also exploited the deep-red luminescence of $[Os(phen)_2(dppz)]^{2+}$ (phen = 1,10-phenanthroline, dppz = dipyridophenazine) for correlative luminescence and transmission electron microscopy (TEM) imaging of nuclear DNA.[21] In this context, the Scattergood and Elliott groups have previously investigated triazole-containing Os^{II} complexes that show lysosomal/endosomal and mitochondrial localisation as optical probes,[22,23] whilst the Thomas group has looked at DNA targeting polypyridyl Os^{II} complexes as high-resolution contrast probes for TEM.[24]

[a]*Department of Chemistry, University of Sheffield, Brook Hill, Sheffield, S3 7HF, UK. E-mail: james.thomas@sheffield.ac.uk*

[b]*Department of Chemistry & Centre for Functional Materials, University of Huddersfield, Queensgate, Huddersfield, HD1 3DH, UK. E-mail: p.i.elliott@hud.ac.uk; p.scattergood@hud.ac.uk*

† Electronic supplementary information (ESI) available. See DOI: 10.1039/d0sc03563g

Yet, whilst there has been interest in Os^{II} complexes as potential anti-cancer therapeutics,[19,25–32] examples of their use in bacteria are far rarer. Despite Dwyer and co-workers reporting the antimicrobial activity of Ru^{II} polypyridyl complexes almost 70 years ago,[33,34] interest in the antibiotic activity of d^6 metal-ion complexes has only returned to some prominence over the last decade.[35–41] However, the use of luminescent complexes for bacterial cell imaging remains a rarity. Following on from its earlier report that a luminescent di-nuclear Ru^{II} complex was taken up by bacteria,[42] the Thomas group recently reported on the antimicrobial activity of di-nuclear analogues against a range of Gram positive and Gram negative bacteria. In these reports, several microscopy techniques were used to investigate cellular internalisation and explore the nature of the interaction of the metal complexes with the bacteria.[43,44] Massi and co-workers have reported cationic Ir^{III}-tetrazolato complexes which show good antimicrobial activity against Gram-positive *D. radiodurans*,[45] whilst charge-neutral members of the same family have also been utilised as molecular probes for the live imaging of *B. cereus*.[46] Whilst there have been some scarce reports of Os^{II} complexes showing inhibition of both Gram-positive and Gram-negative bacteria,[47] to the best of our knowledge, there has yet to be any report that combines luminescence imaging with antimicrobial studies on Os^{II} systems despite their favourable photophysical properties.

Herein we report on the anti-microbial activity of the individual isomers of a family of water-soluble homoleptic Os^{II} complexes featuring 1,2,3-triazole-containing ligands – Scheme 1. Strikingly, it was found that the meridional isomers of these architectures display much greater growth inhibition of Gram-positive bacteria over their facial geometrical isomers. Using the deep-red phosphorescence of these complexes we explore their cellular internalisation and identify their intracellular interaction with DNA.

Results and discussion

Synthesis and characterisation

The previously reported complex $[Os(pytz)_3](PF_6)_2$ $[\mathbf{1}^{2+}](PF_6)_2$ was prepared through an established procedure,[23] which was also used to prepare the related homoleptic complexes $[Os(pymtz)_3](PF_6)_2$ $[\mathbf{2}^{2+}](PF_6)_2$ and $[Os(pyztz)_3][PF_6]_2$ $[\mathbf{3}^{2+}](PF_6)_2$. Briefly, $[OsCl_6][NH_4]_2$ was heated under reflux in ethylene glycol with 3 equivalents of the appropriate ligand, which after counterion metathesis with NH_4PF_6 yielded the hexafluorophosphate salts of the complexes as deep-red coloured solids (Scheme 1).

Due to the asymmetry of the triazole-containing ligands, analysis by ^1H NMR spectroscopy (Fig. S1–S8†) reveals the isolated products to be composed of a mixture of meridional and facial isomers, with formation of the former being favoured in all cases with *mer* : *fac* ratios of 1.4 : 1 ($\mathbf{1}^{2+}$), 2 : 1 ($\mathbf{2}^{2+}$) and 3 : 1 ($\mathbf{3}^{2+}$). Whilst separation of these isomers by column chromatography is challenging, we found that efficient separation is possible on a small scale by employing preparative thin layer chromatography. Metathesis of counterions yielded chloride salts of the separated *fac*- and *mer*-isomers of $\mathbf{1}^{2+}$–$\mathbf{3}^{2+}$ which display excellent aqueous solubility.

The hexafluorophosphate salts of the complexes were analysed by cyclic voltammetry (Fig. 1 and Table 1). The cyclic voltammogram traces for each pair of *mer*- and *fac*-isomers are similar, showing that geometric isomerism has little impact on the electronic properties of the complexes. All complexes exhibit one electrochemically reversible oxidation process attributed to the $Os^{II/III}$ redox couple. Consistent with the increased electron-withdrawing character of each heterocyclic ligand, the potential of this process anodically shifts upon exchange of the pyridyl moiety for pyrimidine and pyrazine. A similar trend was reported recently for a series of bis-terdentate 1,2,3-triazole-based Os^{II} complexes featuring pyridyl and pyrazinyl donors.[48]

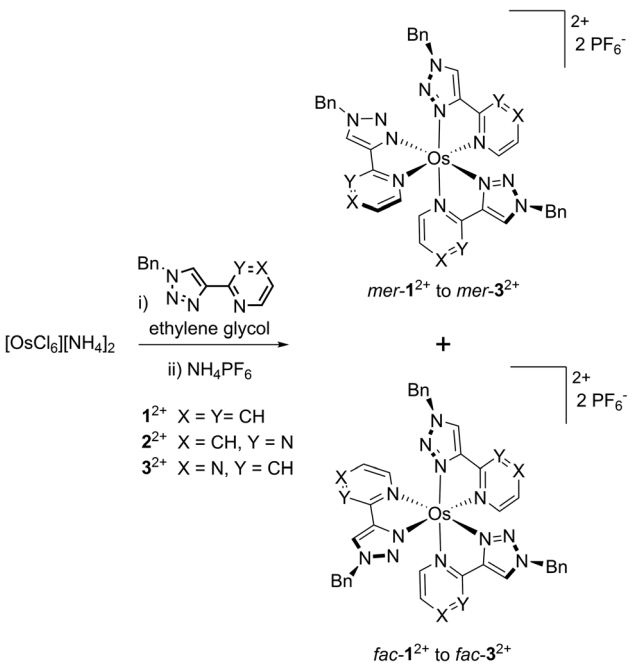

Scheme 1 Synthesis of $\mathbf{1}^{2+}$–$\mathbf{3}^{2+}$.

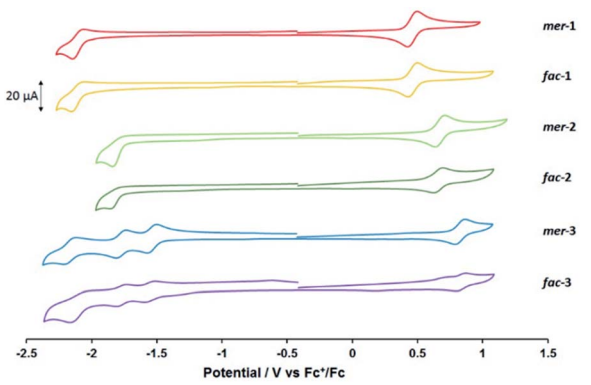

Fig. 1 Cyclic voltammograms recorded at room temperature at 100 mV s^{-1} for 1.0 mmol dm^{-3} MeCN solutions of *mer*- and *fac*-$\mathbf{1}^{2+}$–$\mathbf{3}^{2+}$ as their hexafluorophosphate salts. Solutions contained 0.2 mol dm^{-3} NBu_4PF_6 as supporting electrolyte. All potentials are shown against the Fc^+/Fc couple ($E_{1/2}$ = 0 V).

Table 1 Electrochemical data for 1.0 mmol dm^{-3} MeCN solutions of *mer*- and *fac*-$\mathbf{1}^{2+}$–$\mathbf{3}^{2+}$ as their PF_6^- salts[a]

Complex	E_{ox}/V	E_{red}/V
mer-$\mathbf{1}^{2+}$	+0.46 (73)	−2.10 (87)[b]
fac-$\mathbf{1}^{2+}$	+0.46 (76)	−2.10 (100)[b]
mer-$\mathbf{2}^{2+}$	+0.67 (80)	−1.84[c]
fac-$\mathbf{2}^{2+}$	+0.66 (70)	−1.85[c]
mer-$\mathbf{3}^{2+}$	+0.82 (78)	−1.54 (69), −1.77 (73), −2.17 (98)[b]
fac-$\mathbf{3}^{2+}$	+0.83 (68)	−1.54 (63), −1.77 (73), −2.10 (118)[b]

[a] Measured at room temperature at a scan rate of 100 mV s^{-1}. Potentials are shown *versus* the Fc^+/Fc couple. Anodic–cathodic peak separations ($\Delta E_{a,c}$) for reversible processes are shown in millivolts within brackets. $\Delta E_{a,c}$ for Fc^+/Fc was typically 70 mV. [b] Incompletely-reversible. [c] Irreversible process, cathodic peak potential is quoted.

All the complexes display at least one reduction process within the available electrochemical solvent window. For *mer*- and *fac*-$\mathbf{1}^{2+}$, a reduction which is not completely chemically reversible is observed at −2.10 V *vs.* Fc^+/Fc. By comparison with previous studies on complexes of Os^{II} and Ru^{II} containing this ligand this process is attributed to a ligand-based reduction.[23] Substitution of the pytz ligand with pymtz for both *mer*- and *fac*-$\mathbf{2}^{2+}$ results in the appearance of an irreversible reduction process at more positive potential. This shift is of similar magnitude to the anodic shift in the $Os^{II/III}$ couple relative to $\mathbf{1}^{2+}$, resulting in minimal change in the HOMO–LUMO energy gap. Introduction of a pyrazinyl-donor into the ligand set leads to more complex reductive electrochemistry, with the appearance of two distinct reversible processes at −1.54 and −1.77 V followed by an incompletely chemically reversible couple in the region of −2.1 V *vs.* Fc^+/Fc. These processes are assigned to the successive one-electron reductions of the three coordinated pyztz ligands. Here the anodic shift for the ligand-based reduction is larger than for the Os(II/III) oxidation resulting in a narrowing of the HOMO–LUMO gap.

Density functional theory (DFT) calculations on the *fac*- and *mer*-isomers of $\mathbf{1}^{2+}$ to $\mathbf{3}^{2+}$, carried out using the Orca 4.2 software package,[49,50] confirm the electrochemical data (see Fig. S9, S10 and ESI for details†); in all cases the HOMO has predominantly Os d-orbital character whilst the LUMO is spread over the three ligands (mostly localised over the 6-membered heterocycles) and is of π* character. In agreement with the anodic shift in the oxidation and reduction potentials, the HOMO and LUMO of *fac*/*mer*-$\mathbf{2}^{2+}$ are both stabilised compared to their pyridine-containing analogues resulting in near-identical HOMO–LUMO gaps (*fac*-$\mathbf{1}^{2+}$/$\mathbf{2}^{2+}$ 3.51 eV; *mer*-$\mathbf{1}^{2+}$/$\mathbf{2}^{2+}$ 3.48 eV). For *fac*/*mer*-$\mathbf{3}^{2+}$ the HOMO and LUMO are again stabilised with respect to the pyrimidine-containing complexes but with the latter stabilised to a greater extent, such that the HOMO–LUMO gap is reduced (*fac*-$\mathbf{3}^{2+}$ 3.36 eV; *mer*-$\mathbf{3}^{2+}$ 3.28 eV).

UV-Visible absorption spectra were recorded for the *mer* and *fac* chloride salts of $\mathbf{1}^{2+}$–$\mathbf{3}^{2+}$ in aqueous solution (Fig. 2, Table S1†). Sharp and intense bands observed for all the complexes between 220–300 nm are assigned to singlet ligand-centred (^{1}LC) transitions, whilst bands beyond 350 nm are of MLCT character.

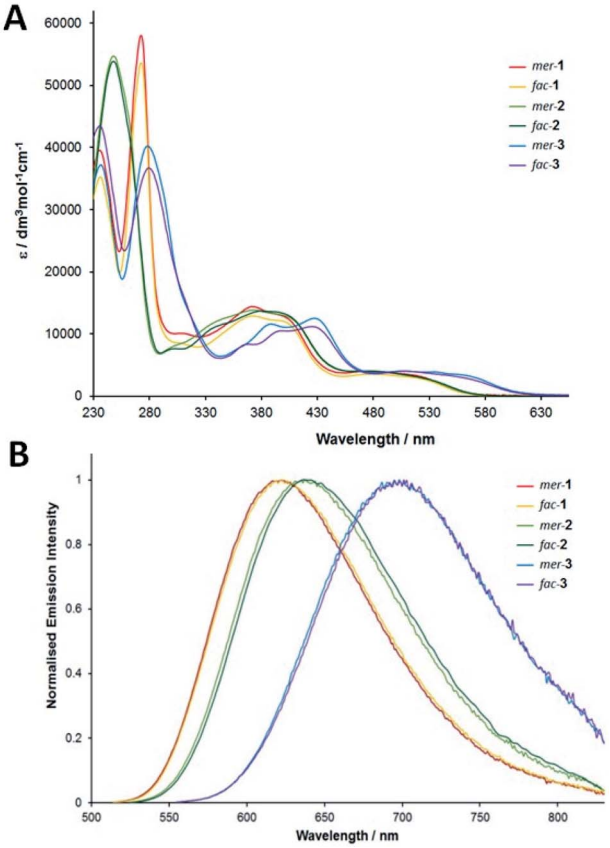

Fig. 2 (A) UV-Visible electronic absorption spectra recorded for aqueous solutions of chloride salts *mer*- and *fac*-$\mathbf{1}^{2+}$–$\mathbf{3}^{2+}$. (B) Normalised photoluminescence spectra recorded for chloride salts *mer*- and *fac*-$\mathbf{1}^{2+}$–$\mathbf{3}^{2+}$ in aerated aqueous solution (λ_{ex} = 500 nm).

Complexes *mer*/*fac*-$\mathbf{1}^{2+}$ and *mer*/*fac*-$\mathbf{2}^{+}$ display a series of bands between 350–420 nm which are attributed to spin-allowed ^{1}MLCT excitations. Weaker bands, still of appreciable intensity, are observed between 430 and 580 nm and are assigned to the expected, formally spin-forbidden, direct excitations to the ^{3}MLCT state.[15,51] In agreement with the electrochemical data, indicating a similar HOMO–LUMO gap for *mer*/*fac*-$\mathbf{1}^{2+}$ and *mer*/*fac*-$\mathbf{2}^{2+}$ (*vide supra*), these bands are near coincident with each other. The analogous transitions for *mer*- and *fac*-$\mathbf{3}^{2+}$ are, however, red-shifted in line with the electrochemical and DFT data.

Time-dependent DFT calculations were carried out for the ground states of all complexes to determine vertical excitation energies and simulate the optical absorption spectra (Fig. S11 and Table S2†). The calculated data are in good agreement with the experimentally measured spectra. Excitations to the S_1 states for $\mathbf{1}^{2+}$ and $\mathbf{2}^{2+}$ are near coincident appearing between 468 (*fac*) and 474 (*mer*) nm whilst those for the isomers of $\mathbf{3}^{2+}$ are red-shifted to 494 (*fac*) and 511 nm (*mer*). In all cases these correspond to transitions predominantly consisting of HOMO → LUMO excitations but have relatively small oscillator strengths and will therefore have little physical significance. The calculated data show that the more intense transitions between 350 and 450 nm correspond to excitations from

Table 2 Photophysical data for chloride salts of *mer*- and *fac*-$\mathbf{1}^{2+}$–$\mathbf{3}^{2+}$ in aqueous solution

	λ_{em}[a]/nm	Φ_{em}[b,d]/% (τ/ns)	Φ_{em}[c,d]/% (τ/ns)
mer-$\mathbf{1}^{2+}$	621	3.9 (365)	7.9 (748)
fac-$\mathbf{1}^{2+}$	623	3.8 (350)	8.4 (715)
mer-$\mathbf{2}^{2+}$	637	2.3 (191)	2.9 (242)
fac-$\mathbf{2}^{2+}$	640	2.5 (171)	3.2 (217)
mer-$\mathbf{3}^{2+}$	696	0.6 (83)	0.6 (92)
fac-$\mathbf{3}^{2+}$	698	0.7 (98)	0.8 (110)

[a] $\lambda_{ex} = 500$ nm. [b] Aerated aqueous solution. [c] N_2-equilibrated aqueous solution. [d] Relative to $[Ru(bpy)_3][PF_6]_2$, $\Phi = 1.8\%$ in aerated MeCN.

orbitals of primarily metal d-orbital character (HOMO-2 to HOMO) with population of ligand-localised orbitals (LUMO up to LUMO+5) confirming the ^{1}MLCT character of the absorption bands in this region. The lowest energy spin-forbidden singlet to triplet transitions appear below the lowest singlet states with the T_1 excitations for $\mathbf{3}^{2+}$ appearing at 560 (*fac*) and 590 (*mer*) nm. In line with expectation, analysis of the compositions of these transitions confirms ^{3}MLCT character.

The chloride salts of all three complexes are luminescent in aerated aqueous solution, exhibiting broad unstructured bands in the red/near-infrared regions of the spectrum attributed to ^{3}MLCT-based emission (Fig. 2B). Again, *mer*- and *fac*-isomerism has almost no effect on the band position within each pair of complexes. In agreement with both the electrochemical and electronic absorbance data (*vide supra*), phosphorescence observed for *mer*/*fac*-$\mathbf{3}^{2+}$ is the most red-shifted in the series. Moderate luminescence lifetimes are observed in aerated aqueous solutions ranging from 83 ns for *mer*-$\mathbf{3}^{2+}$ to 365 ns for *mer*-$\mathbf{1}^{2+}$ (Table 2) with relatively low emission quantum yields of between 0.6 to 3.9%. Trends in both lifetime and quantum yields are in excellent agreement with the energy gap law[52,53] and typical for similar triazole-containing complexes of Os^{II}.[23,48] Quantum yields increase upon deoxygenating the aqueous solutions, supporting assignment to an emissive MLCT state of triplet character. Significantly, the low-energy spin-forbidden absorption envelope of the complexes enables direct population of their ^{3}MLCT states, with emission readily observed using excitation wavelengths as low as 560 (*mer*/*fac*-$\mathbf{1}^{2+}$ and $\mathbf{2}^{2+}$) and 600 nm (*mer*/*fac*-$\mathbf{3}^{2+}$).

The geometries of the lowest-lying triplet states for the complexes were optimised in U-DFT calculations starting from the optimised ground state geometries. In each case the lower energy singly-occupied molecular orbital (SOMO, Fig. S12†) has predominantly Os d-orbital character whilst the excited electron in SOMO+1 is localised primarily on the 6-membered ring of one of the three ligands. This distribution of the SOMO and SOMO+1 confirms the ^{3}MLCT character of these T_1 states further affirmed by Mulliken spin densities of 0.88 to 0.96 for the Os atom.

Cell studies

The cellular uptake properties of the compounds by a range of multi-drug and pan-drug resistant Gram-negative and Gram-positive bacteria were then investigated. In these studies, we chose to investigate a methicillin resistant, clinical isolate strain of the Gram-positive bacterium *Staphylococcus aureus*, MRSA. We compared this to three Gram-negative bacteria strains: a uropathogenic multidrug resistant EC958 ST131 strain of *Escherichia coli*, a multidrug resistant clinical isolate strain of *Pseudomonas aeruginosa* – PA2017 and a multidrug resistant clinical isolate strain of *Acinetobacter baumannii* – AB184. AB184 was selected as it is the most prevalent clonal group of *A. baumannii* in the United Kingdom. In addition, AB184 and PA2017 belong to bacteria groups identified by the World Health Organisation as PRIORITY 1: CRITICAL for developing new antibiotics.[54]

The minimum inhibitory concentration, MIC, of the complexes was obtained in both nutrient rich media Mueller–Hinton-II (MH-II) and defined media – Glucose Defined Minimal Media (GDMM) – in the case of Gram-negative strains and Chemical Defined Media (CDM) for Gram-positive strains. This is the minimum concentration of compound required to halt bacterial cell proliferation. While GDMM has been used in previous studies on metal complexes[55,56] MH-II is closer to relevant biological conditions and is the bacterial growth medium recommended by the European Committee on Antimicrobial Susceptibility Testing. Data is summarised in Table 3.

As with the majority of metal-based antimicrobial compounds[39,45,57] a higher activity against Gram-positive bacteria strains was observed, with all compounds showing no detectable activity on the Gram-negative strains. Strikingly, although complexes $\mathbf{1}^{2+}$ and $\mathbf{2}^{2+}$ exhibit activity against the methicillin resistant strain of *S. aureus*, in both cases their *mer* isomer is most active, with *mer*-$\mathbf{1}^{2+}$ being comparable to standard antibiotics. More significantly still, this activity is not reduced in a pathogenic strain resistant to methicillin and ampicillin.

In recent studies, the antimicrobial activity of the direct Ru^{II} analogue of $\mathbf{1}^{2+}$ has been investigated. The Crowley group reported that both the *mer* and *fac* isomers of its hexafluorophosphate salt showed very low activity against wild-type *S. aureus*.[39] This observation is probably due to the low water

Table 3 MIC (μg mL^{-1}) results for *E. coli* pathogenic (EC958), *S. aureus* pathogenic (MRSA), *A. baumannii* pathogenic (AB184) and *P. aeruginosa* pathogenic (PA2017) strains in minimal media and MH-II

	mer-$\mathbf{1}^{2+}$	*fac*-$\mathbf{1}^{2+}$	*mer*-$\mathbf{2}^{2+}$	*fac*-$\mathbf{2}^{2+}$	*mer*-$\mathbf{3}^{2+}$	*fac*-$\mathbf{3}^{2+}$	Control[a]
Defined minimal media							
EC958	>512	>512	>512	>512	>512	>512	>512
PA2017	>512	>512	>512	>512	>512	>512	>512
MRSA	32	256	64	128	>512	>512	>512
AB184	>512	>512	256	>512	256	>512	>512
Mueller–Hinton-II							
EC958	>512	>512	>512	>512	>512	>512	>512
PA2017	>512	>512	>512	>512	>512	>512	>512
MRSA	48	256	128	256	>512	>512	>512
AB184	>512	>512	256	>512	>512	>512	>512

[a] Ampicillin used as control.

solubility of such salts as a more recent study on the unseparated isomers of this complex, as a chloride salt, showed good activity against the non-pathogenic Gram-positive bacteria *Bacillus subtilis* and *Staphylococcus epidermidis.*[58] The Crowley group have also varied the identity of the triazole substituent within these Ru^{II} systems, reporting that those bearing *n*-hexyl and *n*-octyl groups are the most potent against wild-type *S. aureus*.[39] The chloride salts of these two complexes were then investigated against a wider panel of bacteria, which revealed that this activity was retained in pathogenic MRSA strains. However, as both the hexafluorophosphate and chloride salts display similar MIC figures against wild-type *S. aureus*, their activity is attributed to an optimisation of lipophilicity, rather than solubility. Promising antimicrobial activity has also been observed in related Ru^{II} analogues incorporating isoquinoline appended triazole ligands,[58] and in quinoline-based Ru^{II} systems featuring tetrazole moieties.[59] Interestingly, in the latter case, the *fac*-isomers are more active than their *mer*-analogues. Although structurally similar to the Os^{II} systems reported herein, the subtle increase in hydrophobicity achieved through inclusion of the extended aromatic units within the coordinated ligands is likely to be responsible for the improved potency of both of these architectures against both Gram-positive and Gram-negative bacteria, certainly a similar effect is observed in Ru^{II} complexes incorporating the alkylated ligands described above.[39]

To determine whether the complexes cause bacterial cell death or just halt bacterial proliferation, estimates of minimum bactericidal concentration, MBC, were obtained and these data are summarised in Table 4. As with the MIC experiments, the *mer* isomers are the most active with *mer*-$\mathbf{1}^{2+}$ exhibiting the highest potency. The MBC values of all compounds lie within a 4-fold window of the MIC values, revealing that the compounds are classically bactericidal.

Given that osmium complexes have been more widely targeted as photodynamic therapy agents,[19,28,60] the phototoxic effects of the compounds towards the pathogenic, Gram-positive bacteria *S. aureus*, MRSA strain were also studied (see Fig. S13†). Bacterial cell survival following exposure to each compound was determined upon exposure to different light fluences (0, 8 and 48 J cm^{-2}) and compared to a control in the dark. These data show that, for the majority of complexes, low light fluences do not result in increased antibacterial activity. However, at higher light fluences a detectable but small increase in activity (phototoxic index: ~2) was observed. As with the previous studies *mer*-$\mathbf{1}^{2+}$ exhibited the highest phototoxicity. As *mer*-$\mathbf{1}^{2+}$ appeared to be the most promising therapeutic in all the assays, we further explored its activity and mechanism of action and compared to its corresponding *fac*-isomer.

By exploiting the emission properties of $\mathbf{1}^{2+}$ we investigated its cellular uptake and localisation using Structured Illumination Microscopy (SIM),[61–63] a super-resolution technique that allows for improved resolutions up to 100 nm. SIM imaging with *S. aureus* (MRSA strain) indicated that *mer*-$\mathbf{1}^{2+}$ is cell-permeant (Fig. 3). These images indicate that, 60 minutes after exposure to *mer*-$\mathbf{1}^{2+}$, staining to cell membranes and bacterial DNA occurs (see Fig. S14† for intracellular luminescence intensity plots). However, after 120 minutes, accumulation within bacterial DNA predominates which is particularly apparent in 3D projections. The DNA appears to be condensed which may be an indication of DNA damage.

The uptake properties of *fac*-$\mathbf{1}^{2+}$ in the same MRSA strain was also investigated (see Fig. S15†). As with *mer*-$\mathbf{1}^{2+}$, *fac*-$\mathbf{1}^{2+}$ initially stains both the membranes and intracellular DNA of the

Table 4 MBC (μg mL^{-1}) results for *E. coli* pathogenic (EC958), *S. aureus* pathogenic (MRSA), *A. baumannii* pathogenic (AB184) and *P. aeruginosa* pathogenic (PA2017) strains in minimal media and MH-II

	mer-$\mathbf{1}^{2+}$	*fac*-$\mathbf{1}^{2+}$	*mer*-$\mathbf{2}^{2+}$	*fac*-$\mathbf{2}^{2+}$	*mer*-$\mathbf{3}^{2+}$	*fac*-$\mathbf{3}^{2+}$	Control[a]
Defined minimal media							
EC958	>512	>512	>512	>512	>512	>512	>512
PA2017	>512	>512	>512	>512	>512	>512	>512
MRSA	48	256	96	256	512	512	>512
AB184	>512	>512	512	512	512	512	>512
Mueller–Hinton-II							
EC958	>512	>512	>512	>512	>512	>512	>512
PA2017	>512	>512	>512	>512	>512	>512	>512
MRSA	128	256	256	256	512	512	>512
AB184	>512	>512	256	>512	>512	>512	>512

[a] Ampicillin used as control.

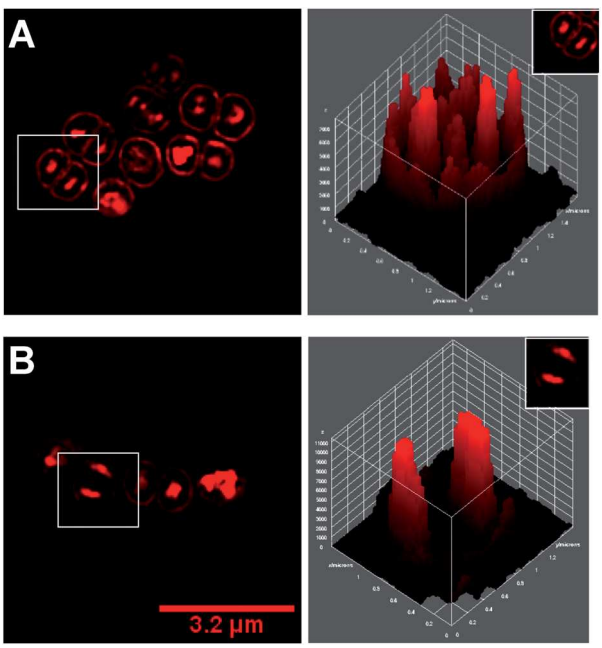

Fig. 3 Uptake of complex *mer*-$\mathbf{1}^{2+}$ by *S. aureus* MRSA cells monitored through SIM microscopy. *S. aureus* (MRSA strain) cells were incubated with MIC concentrations of *mer*-$\mathbf{1}^{2+}$ for 60 (A) and 120 (B) minutes. Left: cross-section through the centre of the cell where peak intensity was observed. Right: 3D surface plots of selected cells in the area of the white box shown in cross-section image, revealing membrane and nuclear staining at 60 min and solely nuclear staining at 120 min. Emission was collected in the A458 channel upon excitation with the 405 nm laser. Cells were fixed using paraformaldehyde (4%) and washed in PBS. Cells were mounted using Slowfade Gold Antifade.

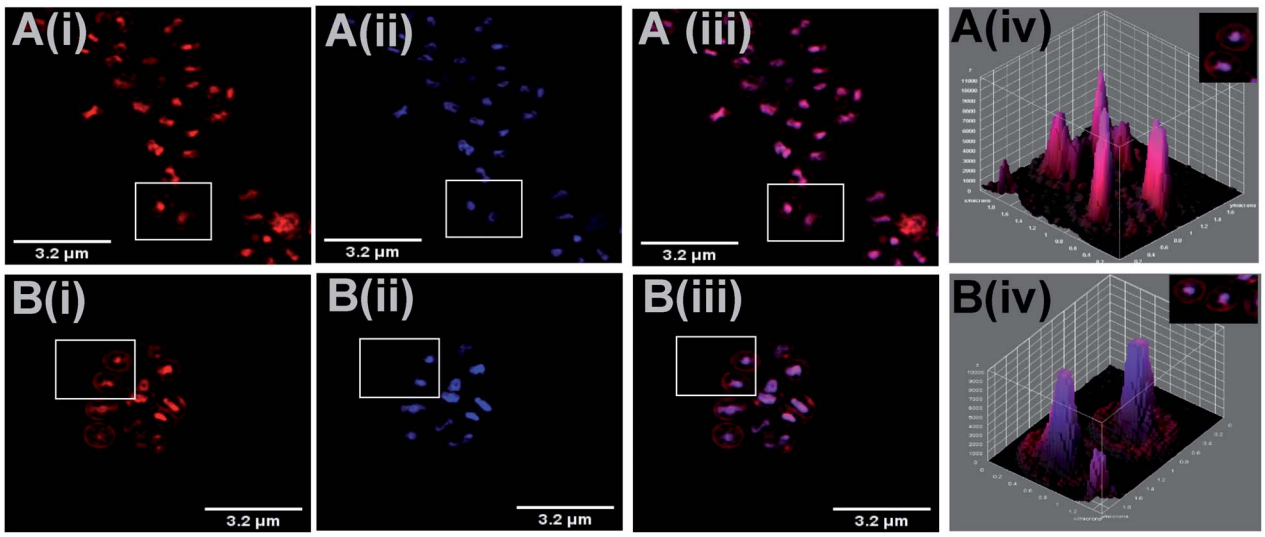

Fig. 4 3D *Z*-stack projection, SIM colocalisation study using *S. aureus* MRSA after 1 hour incubation of cells with MIC concentrations of *fac*-$\mathbf{1}^{2+}$ (A) and *mer*-$\mathbf{1}^{2+}$ (B). (i) Image obtained on excitation of $\mathbf{1}^{2+}$ collected in the A568 channel. (ii) Images obtained by simultaneous staining with DAPI, collected in the DAPI channel. (iii) Overlay of both channels. (iv) 3D surface plots for the selected cells shown in the corresponding white boxes of the colocalisation images, showing emission intensity for $\mathbf{1}^{2+}$ and DAPI.

bacteria, although there is significantly less membrane localisation. Again, after two hours, it largely accumulates within the bacterial DNA. Intriguingly, measured distances between the membrane, DNA and cell septum for compounds stained with the *fac*-isomer were smaller on average than those for cells exposed to *mer*-$\mathbf{1}^{2+}$, suggesting that uniquely *mer*-$\mathbf{1}^{2+}$ causes cell swelling, perhaps as a consequence of the cell death mechanism it provokes.

To confirm DNA localisation, co-staining experiments were carried out with the DNA stain DAPI (4′,6-diamidino-2-phenylindole, Fig. 4).[64] These images show a direct overlay between the emission of DAPI and both complexes within the bacterial DNA, which is clearly seen in the corresponding 3D surface projections and also reflected in their high Pearson's coefficients (*fac*-$\mathbf{1}^{2+} = 0.95$; *mer*-$\mathbf{1}^{2+} = 0.92$). As with the previous imaging experiments, it is clear that cells stained with the *mer*-isomer are noticeably swollen.

Cell-free binding titrations on both isomers of $\mathbf{1}^{2+}$ using their DNA-induced increase in steady-state emission (see Fig. S16†), reveal they both bind to duplex DNA with relatively low affinities of K_b(*fac*-$\mathbf{1}^{2+}$) $= 4.1 \times 10^5$ M^{-1} and K_b(*mer*-$\mathbf{1}^{2+}$) $= 9.8 \times 10^4$ M^{-1}. However, as the DNA binding affinity of *fac*-$\mathbf{1}^{2+}$ is actually slightly higher than the more therapeutically active *mer*-$\mathbf{1}^{2+}$ it seems that this is, at best, only one factor in the cell death mechanism. It has been suggested that the mechanism of action of the previously discussed Ru^{II} analogues of $\mathbf{1}^{2+}$, is due to membrane disruption and no DNA localisation was observed. However, these systems incorporate more lipophilic ligands and it is known that such physiochemical changes enhance binding to membranes over nucleic acids.[65,66]

To investigate any difference in internalisation, the uptake properties of both isomers were investigated using ICP-AES (inductively coupled plasma atomic emission spectroscopy, Fig. 5). Uptake experiments were conducted in the absence of glucose over the course of an hour, as the imaging studies showed both compounds accumulate within bacteria over this period.

The ICP-AES experiments reveal that overall the *mer*-isomer is preferentially taken up by *S. aureus*. In addition, the uptake profiles of the isomers are different; initially, *fac*-$\mathbf{1}^{2+}$ concentrations increase quite rapidly but uptake plateaus between 10 and 20 minutes. In contrast, the uptake of *mer*-$\mathbf{1}^{2+}$ is rapid for 5 minutes and although the uptake rate then decreases, the concentration of *mer*-$\mathbf{1}^{2+}$ continues to rise for the entire 60 minutes of the experiment. The differential uptake of *mer*-$\mathbf{1}^{2+}$ and *fac*-$\mathbf{1}^{2+}$ is consistent with their observed activities and the brighter emission intensity of *mer*-$\mathbf{1}^{2+}$ within cells.

The experiment was repeated with *E. coli*, EC958, to investigate whether any change in uptake between Gram-positive and Gram-negative bacteria affected the observed differences in activity. As illustrated in Fig. 5, both complexes show levels of

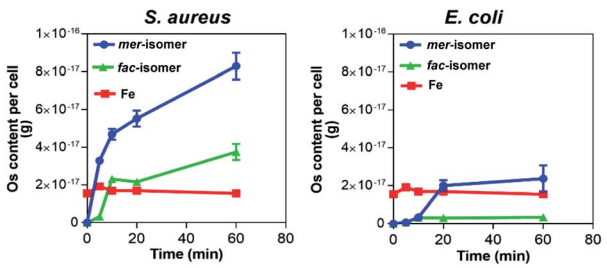

Fig. 5 ICP-AES accumulation data for the uptake of osmium by *S. aureus* (MRSA) (left) and *E. coli* (EC958) (right), in the absence of glucose after exposure to *mer*-$\mathbf{1}^{2+}$ (blue) and *fac*-$\mathbf{1}^{2+}$ (green). [Fe] levels were calculated as a control (red). Os and Fe levels are expressed as metal (g) per cell. Compounds were added at MIC concentration in GDMM. Cells were washed with 0.5% (v/v) nitric acid to remove unbound complex. Error bars represent three independent biological repeats ± SD.

uptake in *E. coli* which reflects their lowered activity in this Gram-negative species. Indeed, SIM experiments with EC958, showed little or no detectable uptake of either complex, as their emission was too weak to produce image reconstructions.

Conclusions

We have presented the synthesis and photophysical study of new osmium(II)-based complexes and their cellular uptake and antimicrobial activities against clinically relevant bacterial strains. The meridional isomer of $\mathbf{1}^{2+}$ exhibited the highest antimicrobial activity which was competitive with conventional antibiotics and was active against methicillin- and ampicillin-resistant pathogenic *S. aureus*. Further, these antimicrobial studies were combined with super-resolution imaging studies using the red phosphorescence for $\mathbf{1}^{2+}$ which demonstrated a high degree of bacterial DNA localisation. As $\mathbf{1}^{2+}$ undergoes quenching of emission in the presence of air through generation of $^1O_2$ the light-induced toxicity was investigated, resulting in the determination of a modest phototoxic index of 2. Fascinatingly, the *fac* and *mer* isomers of $\mathbf{1}^{2+}$ display distinct differences in their biological properties, with *mer*-$\mathbf{1}^{2+}$ exhibiting both higher antibacterial activity and brighter cell staining properties. These differences are due to the higher cell uptake of this isomer compared to *fac*-$\mathbf{1}^{2+}$.

Complexes of osmium(II) have attractive photophysical properties for biological and biomedical applications with prominent low energy absorption bands for direct ground state to ^{3}MLCT state transitions and deep-red to near-IR emission. This enables increased depth of penetration in tissues for excitation with low energy light, imaging and $^1O_2$ sensitisation. The results presented here therefore demonstrate the significant potential for Os(II) complexes in (photo)therapeutic antimicrobial applications.

Conflicts of interest

There are no conflicts to declare.

Acknowledgements

P. I. P. E. and P. A. S. acknowledge the University of Huddersfield for supporting this research as well as Dr Steve Andrews (3M Business and Innovation Centre, University of Huddersfield) for computational resources used in this work. KS is grateful to the BBSRC for a Ph.D. studentship through the White Rose Structural Biology DTP. Imaging work was performed at the Wolfson Light Microscopy Facility, using a DeltaVision/GE OMX optical microscope, funded by MRC grant MK/K0157531/1.

Notes and references

1 C. Metcalfe and J. A. Thomas, *Chem. Soc. Rev.*, 2003, **32**, 215–310.
2 K. K.-W. Lo, W.-K. Hui, C.-K. Chung, K. H.-K. Tsang, D. C.-M. Ng, N. Zhu and K.-K. Cheung, *Coord. Chem. Rev.*, 2005, **249**, 1434–1450.
3 K. K.-W. Lo, M.-W. Louie and K. Y. Zhang, *Coord. Chem. Rev.*, 2010, **254**, 2603–2622.
4 M. R. Gill and J. A. Thomas, *Chem. Soc. Rev.*, 2012, **41**, 3179–3192.
5 M. P. Coogan and V. Fernández-Moreira, *Chem. Commun.*, 2013, **50**, 384.
6 K. K.-W. Lo, *Acc. Chem. Res.*, 2015, **48**, 2985–2995.
7 F. E. Poynton, S. A. Bright, S. Blasco, D. C. Williams, J. M. Kelly and T. Gunnlaugsson, *Chem. Soc. Rev.*, 2017, **36**, 1–51.
8 J. D. Knoll, B. A. Albani and C. Turro, *Acc. Chem. Res.*, 2015, **48**, 2280–2287.
9 F. Heinemann, J. Karges and G. Gasser, *Acc. Chem. Res.*, 2017, **50**, 2727–2736.
10 J. Liu, C. Zhang, T. W. Rees, L. Ke, L. Ji and H. Chao, *Coord. Chem. Rev.*, 2018, **363**, 17–28.
11 S. Monro, K. L. Colón, H. Yin, J. Roque III, P. Konda, S. Gujar, R. P. Thummel, L. Lilge, C. G. Cameron and S. A. McFarland, *Chem. Rev.*, 2018, **119**, 797–828.
12 D. E. J. G. J. Dolmans, D. Fukumura and R. K. Jain, *Nat. Rev. Cancer*, 2003, **3**, 380–387.
13 W. Fan, P. Huang and X. Chen, *Chem. Soc. Rev.*, 2016, **45**, 6488–6519.
14 G. Lemercier, M. Four and S. Chevreux, *Coord. Chem. Rev.*, 2018, **368**, 1–12.
15 F. Felix, J. Ferguson, H. U. Güdel and A. Ludi, *Chem. Phys. Lett.*, 1979, **62**, 153–157.
16 P. Zhang and H. Huang, *Dalton Trans.*, 2018, **47**, 14841–14854.
17 A. Byrne, C. N. Dolan, R. D. Moriarty, A. Martin, U. Neugebauer, R. J. Forster, A. Davies, Y. Volkov and T. E. Keyes, *Dalton Trans.*, 2015, **44**, 14323–14332.
18 K. S. Gkika, A. Byrne and T. E. Keyes, *Dalton Trans.*, 2019, **48**, 17461–17471.
19 P. Zhang, Y. Wang, K. Qiu, Z. Zhao, R. Hu, C. He, Q. Zhang and H. Chao, *Chem. Commun.*, 2017, **53**, 12341–12344.
20 C. Ge, H. Huang, Y. Wang, H. Zhao, P. Zhang and Q. Zhang, *ACS Appl. Bio Mater.*, 2018, **1**, 1587–1593.
21 R. Huang, F.-P. Feng, C.-H. Huang, L. Mao, M. Tang, Z.-Y. Yan, B. Shao, L. Qin, T. Xu, Y.-H. Xue and B.-Z. Zhu, *ACS Appl. Mater. Interfaces*, 2020, **12**, 3465–3473.
22 S. A. E. Omar, P. A. Scattergood, L. K. McKenzie, H. E. Bryant, J. A. Weinstein and P. I. P. Elliott, *Molecules*, 2016, **21**, 1382–1412.
23 S. A. E. Omar, P. A. Scattergood, L. K. McKenzie, C. Jones, N. J. Patmore, A. J. H. M. Meijer, J. A. Weinstein, C. R. Rice, H. E. Bryant and P. I. P. Elliott, *Inorg. Chem.*, 2018, **57**, 13201–13212.
24 A. Wragg, M. R. Gill, C. J. Hill, X. Su, A. J. H. M. Meijer, C. Smythe and J. A. Thomas, *Chem. Commun.*, 2014, **50**, 14494–14497.
25 J. Maksimoska, D. S. Williams, G. E. Atilla-Gokcumen, K. S. M. Smalley, P. J. Carroll, R. D. Webster, P. Filippakopoulos, S. Knapp, M. Herlyn and E. Meggers, *Chem. –Eur. J.*, 2008, **14**, 4816–4822.
26 N. P. E. Barry, F. Edafe, P. J. Dyson and B. Therrien, *Dalton Trans.*, 2010, **39**, 2816.

27 Y. Fu, A. Habtemariam, A. M. Pizarro, S. H. van Rijt, D. J. Healey, P. A. Cooper, S. D. Shnyder, G. J. Clarkson and P. J. Sadler, *J. Med. Chem.*, 2010, **53**, 8192–8196.
28 Y. Sun, L. E. Joyce, N. M. Dickson and C. Turro, *Chem. Commun.*, 2010, **46**, 6759.
29 S. H. V. Rijt, H. Kostrhunova, V. Brabec and P. J. Sadler, *Bioconjugate Chem.*, 2011, **22**, 218–226.
30 K. Suntharalingam, T. C. Johnstone, P. M. Bruno, W. Lin, M. T. Hemann and S. J. Lippard, *J. Am. Chem. Soc.*, 2013, **135**, 14060–14063.
31 Y. Fu, M. J. Romero, L. Salassa, X. Cheng, A. Habtemariam, G. J. Clarkson, I. Prokes, A. Rodger, G. Costantini and P. J. Sadler, *Angew. Chem., Int. Ed.*, 2016, **55**, 8909–8912.
32 C. C. Konkankit, S. C. Marker, K. M. Knopf and J. J. Wilson, *Dalton Trans.*, 2018, **47**, 9934–9974.
33 F. P. Dwyer, E. C. Gyarfas, W. P. Rogers and J. H. Koch, *Nature*, 1952, **170**, 190–191.
34 F. P. Dwyer, A. Shulman, G. M. Laycock and S. Dixson, *Aust. J. Exp. Biol. Med. Sci.*, 1969, **47**, 203–218.
35 A. Regiel-Futyra, J. M. Dąbrowski, O. Mazuryk, K. Śpiewak, A. Kyzioł, B. Pucelik, M. Brindell and G. Stochel, *Coord. Chem. Rev.*, 2017, **351**, 76–117.
36 X. Li, A. K. Gorle, M. K. Sundaraneedi, F. R. Keene and J. G. Collins, *Coord. Chem. Rev.*, 2018, **375**, 134–147.
37 A. Bolhuis, L. Hand, J. E. Marshall, A. D. Richards, A. Rodger and J. Aldrich-Wright, *Eur. J. Pharm. Sci.*, 2011, **42**, 313–317.
38 L. Lu, L.-J. Liu, W. C. Chao, H.-J. Zhong, M. Wang, X. P. Chen, J. J. Lu, R. N. Li, D.-L. Ma and C.-H. Leung, *Sci. Rep.*, 2015, **5**, 14544–14549.
39 S. V. Kumar, S. Ø. Scottwell, E. Waugh, C. J. McAdam, L. R. Hanton, H. J. L. Brooks and J. D. Crowley, *Inorg. Chem.*, 2016, **55**, 9767–9777.
40 P. Srivastava, M. Shukla, G. Kaul, S. Chopra and A. K. Patra, *Dalton Trans.*, 2019, **48**, 11822–11828.
41 A. Frei, J. Zuegg, A. G. Elliott, M. Baker, S. Braese, C. Brown, F. Chen, C. G. Dowson, G. Dujardin, N. Jung, A. P. King, A. M. Mansour, M. Massi, J. Moat, H. A. Mohamed, A. K. Renfrew, P. J. Rutledge, P. J. Sadler, M. H. Todd, C. E. Willans, J. J. Wilson, M. A. Cooper and M. A. T. Blaskovich, *Chem. Sci.*, 2020, **11**, 2627–2639.
42 M. R. Gill, J. Garcia-Lara, S. J. Foster, C. Smythe, G. Battaglia and J. A. Thomas, *Nat. Chem.*, 2009, **1**, 662–667.
43 K. L. Smitten, H. M. Southam, J. Bernardino de la Serna, M. R. Gill, P. J. Jarman, C. G. W. Smythe, R. K. Poole and J. A. Thomas, *ACS Nano*, 2019, **13**, 5133–5146.
44 K. L. Smitten, S. D. Fairbanks, C. C. Robertson, J. Bernardino de la Serna, S. J. Foster and J. A. Thomas, *Chem. Sci.*, 2020, **11**, 70–79.
45 V. Fiorini, I. Zanoni, S. Zacchini, A. L. Costa, A. Hochkoeppler, V. Zanotti, A. M. Ranieri, M. Massi, A. Stefan and S. Stagni, *Dalton Trans.*, 2017, **46**, 12328–12338.
46 A. M. Ranieri, C. Caporale, V. Fiorini, A. Hubbard, P. Rigby, S. Stagni, E. Watkin, M. I. Ogden, M. J. Hackett and M. Massi, *Chem. –Eur. J.*, 2019, **25**, 10566–10570.
47 E. Menéndez-Pedregal, Á. Manteca, J. Sánchez, J. Díez, M. P. Gamasa and E. Lastra, *Eur. J. Inorg. Chem.*, 2015, **2015**, 1424–1432.
48 P. A. Scattergood, J. Roberts, S. A. E. Omar and P. I. P. Elliott, *Inorg. Chem.*, 2019, **58**, 8607–8621.
49 F. Neese, *Wiley Interdiscip. Rev.: Comput. Mol. Sci.*, 2011, **2**, 73–78.
50 F. Neese, *Wiley Interdiscip. Rev.: Comput. Mol. Sci.*, 2017, **8**, 33–36.
51 E. M. Kober and T. J. Meyer, *Inorg. Chem.*, 1982, **21**, 3967–3977.
52 J. V. Caspar, E. M. Kober, B. P. Sullivan and T. J. Meyer, *J. Am. Chem. Soc.*, 1982, **104**, 630–632.
53 E. M. Kober, J. V. Caspar, R. S. Lumpkin and T. J. Meyer, *J. Phys. Chem.*, 1986, **90**, 3722–3734.
54 E. Tacconelli, E. Carrara, A. Savoldi, S. Harbarth, M. Mendelson, D. L. Monnet, C. Pulcini, G. Kahlmeter, J. Kluytmans, Y. Carmeli, M. Ouellette, K. Outterson, J. Patel, M. Cavaleri, E. M. Cox, C. R. Houchens, M. L. Grayson, P. Hansen, N. Singh, U. Theuretzbacher, N. Magrini, S. S. Al-Abri, N. Awang Jalil, N. Benzonana, S. Bhattacharya, F. R. Burkert, O. Cars, G. Cornaglia, S. Gandra, C. G. Giske, D. A. Goff, M. Guzman Blanco, T. Jinks, S. S. Kanj, L. Kerr, M.-P. Kieny, K. Leder, G. Levy-Hara, J. Littman, S. Malhotra-Kumar, A. Pan, D. L. Paterson, M. Paul, J. Rodríguez-Baño, M. Sanguinetti, S. Sengupta, M. Sharland, M. Si-Mehand, L. L. Silver, G. E. Thwaites, J. W. van der Meer, S. Vega, A. Wechsler-Fördös, N. Woodford, F. O. Yilmaz and A. Zorzet, *Lancet Infect. Dis.*, 2018, **18**, 318–327.
55 J. Flatley, J. Barrett, S. T. Pullan, M. N. Hughes, J. Green and R. K. Poole, *J. Biol. Chem.*, 2005, **280**, 10065–10072.
56 H. M. Southam, J. A. Butler, J. A. Chapman and R. K. Poole, *Adv. Microb. Physiol.*, 2017, **71**, 1–96.
57 F. Li, Y. Mulyana, M. Feterl, J. M. Warner, J. G. Collins and F. R. Keene, *Dalton Trans.*, 2011, **40**, 5032.
58 N. W. Kreofsky, M. D. Dillenburg, E. M. Villa and J. T. Fletcher, *Polyhedron*, 2020, **177**, 114259.
59 N. Monti, S. Zacchini, M. Massi, A. Hochkoeppler, L. Giorgini, V. Fiorini, A. Stefan and S. Stagni, *Appl. Organomet. Chem.*, 2020, **34**, e5806.
60 S. Lazic, P. Kaspler, G. Shi, S. Monro, T. Sainuddin, S. Forward, K. Kasimova, R. Hennigar, A. Mandel, S. McFarland and L. Lilge, *Photochem. Photobiol.*, 2017, **93**, 1248–1258.
61 M. Gustafsson, *J. Microsc.*, 2000, **198**, 82–87.
62 L. Shao, P. Kner, E. H. Rego and M. G. L. Gustafsson, *Nat. Methods*, 2011, **8**, 1044–1046.
63 R. Fiolka, L. Shao, E. H. Rego, M. W. Davidson and M. G. L. Gustafsson, *Proc. Natl. Acad. Sci. U. S. A.*, 2012, **109**, 5311–5315.
64 J. Kapuscinski, *Biotech. Histochem.*, 1995, **70**, 220–233.
65 M. R. Gill, D. Cecchin, M. G. Walker, R. S. Mulla, G. Battaglia, C. Smythe and J. A. Thomas, *Chem. Sci.*, 2013, **4**, 4512–4519.
66 A. C. Komor and J. K. Barton, *Chem. Commun.*, 2013, **49**, 3617–3630.